Petroleum 6 (2020) 198–205

Contents lists available at ScienceDirect

Petroleum

journal homepage: http://www.keaipublishing.com/en/journals/petroleum

A tight sandstone multi-physical hydraulic fractures simulator study and its field application

Yonghong Wang[a,b], Binshan Ju[a], Shihao Wang[c,*], Zhenzhou Yang[b], Qing Liu[b]

[a] School of Energy Resource, China University of Geoscience, Beijing, China
[b] CNPC Engineering Technology R&D Company Limited (CPET), China
[c] Petroleum Engineering Department, Colorado School of Mines, Golden, CO, 80401, USA

ARTICLE INFO

Keywords:
Tight sandstone ;
Hydraulic fracture simulator ;
Integrated finite difference discretization ;
Stress contrast

ABSTRACT

During the past years, the recovery of unconventional gas formation has attracted lots of attention and achieved huge success. To produce gas from the low-permeability unconventional formations, hydraulic fracturing technology is essential and critical. In this paper, we present the development of a three-dimensional thermal-hydraulic-mechanical numerical simulator for the simulation of hydraulic fracturing operations in tight sandstone reservoirs. Our simulator is based on integrated finite difference (IFD) method. In this method, the simulation domain is subdivided into sub domains and the governing equations are integrated over a sub domain with flux terms expressed as an integral over the sub domain boundary using the divergence theorem. Our simulator conducts coupled thermal-hydraulic-mechanical simulation of the initiation and extension of hydraulic fractures. It also calculates the mass/heat transport of injected hydraulic fluids as well as proppants. Our simulator is able to handle anisotropic formations with multiple layers. Our simulator has been validated by comparing with an analytical solution as well as Ribeiro and Sharma model. Our model can simulate fracture spacing effect on fracture profile when combining IFD with Discontinuous Displacement Method (DDM).

1. Introduction

The numerical approaches to quantify the performance of hydraulic fracturing operations have been investigated since the 1960s. Perkins and Kern [1], who applied the plane strain crack solution by Sneddon [2], developed the earliest hydraulic fracturing model, called the PK model. The PK model was later extended by Nordgren to PKN model [3]. In the PKN model, the fractures are assumed to be long and with constant height and elliptical cross-section. Geertsma and De Klerk developed the KGD model in 1969, which assumes the fractures to be short and to be under plain strain. Clearly, PKN and KGD models are rough estimations of the fracture geometry. For the field applications in complex multi-layer reservoirs, three-dimensional models of hydraulic fractures with fluid/proppant transport are demanding. To simulate several numerical approaches have been developed.

Finite Element Method (FEM) has been widely used in fracture mechanics [5–7]. Traditional FEM needs frequent remeshing to accurately capture the dynamic growth of the fracture. Extended Finite Element Method (XFEM) resolves this issue [8–10]. XFEM adopts an 'enriched' base function and the Partition of Unity Method (PUM) to enable crack inside an element. In this way, XFEM resolves the difficulty of remeshing. Recently, XFEM has been successfully used to model hydraulic fracturing [11–13]. Although XFEM is very flexible in handing fracture extensions, it has to discretize and solve the entire computational domain (formation in our case), which prevents it from being applied in field-scale simulation, especially real-time simulation.

Recently, Wu and Olson developed a multistage fracturing simulator based on Discontinuous Discontinuity Method (DDM) [14–16], and conduct Numerical Investigation of complex fracture networks in naturally fractured reservoirs. DDM is essentially an extension of Boundary Element Method (DEM), which is based on analytical solution of point source and Green's theorem. DDM is the solution of plane elasticity problems by the displacement discontinuity method [17], which solves the computational domain on the boundary only, reducing a 3D problem to a 2D one. In this sense, DDM is naturally suitable of the growth of hydraulic fractures with relatively less computational resources. Li developed a fully coupled thermal-hydraulic-mechanical hydraulic-fracturing simulator based on mixed finite-volume/finite element method [18]. The simulator has been used to simulate multistage fracturing and has achieved good performance. However, the

Peer review under responsibility of Southwest Petroleum University.
* Corresponding author.
E-mail address: 631427988@qq.com (S. Wang).

https://doi.org/10.1016/j.petlm.2019.05.001
Received 4 December 2018; Received in revised form 29 April 2019; Accepted 23 May 2019

model does not account for the proppant transport in the fracture. Wu and Olson have extended DDM to simulate the interaction between hydraulic fractures and natural fractures [19]. Later, Tang combined DDM with Finite Difference Method to account for the transport of fluid/proppant in the fracture systems in 2016 [20]. Prashanth optimize multiple fractures propagating simultaneously in hydraulic fracturing to achieve uniform growth using data-based model reduction in 2018 [21]. Guo develop a Reservoir-Geomechanics-Fracturing Model to analyze the Effects of Subsequent Parent Well Injection on Interwell Fracturing Interference in 2018 [22]. Yu develop a numerical model to simulate pressure response of well interference and well performance in tight oil reservoir by fast embedded-discrete-fracture-model (EDFM) method in 2018, the fracture model is complex fracture geometries. And simulate shale gas transport and production with complex fractures model [23,24].

In this paper, we have developed a multi-physical hydraulic fractures simulator for tight sandstone, and solve fractures model by Integrated Finite Difference Discretization (IFD), which is easy to get convergent solution and save calculation time based on our analyses. Our simulator can calculate the mass/heat transport of injected hydraulic fluids as well as proppants, and handle anisotropic formations with multiple layers, analyze different mudstone/shale layer, stress contrast and fractures spacing effect for fractures extension.

2. Mathematical model

2.1. Fracture mechanics

As we know, the injection of fracturing fluids builds up the downhole pressure and consequently causes the formation to fail. There are several models to describe the failure of rock, namely Mode-1 failure (tearing), Mode-2 failure (shearing) and Mode-3 failure (hybrid model). At the time being, we only consider Mode-1 failure, the stress intensity factor at the fracture tip is as shown in Equation (1), [25].

$$K_I = \frac{E}{8(1-\upsilon^2)}\left(\frac{2\pi}{r}\right)^{1/2} w_{fr}(r) \tag{1}$$

where K_I is the stress intensity factor at the fracture tip and r is the inward normal distance from the fracture front. $\upsilon$is the Poisson's ratio. $w_{fr}$is the width of the fracture front.

The velocity at which the fracture front extension can be calculated as [26]:

$$v_{front} = C_{ext}\left(\frac{K_I - K_{IC}}{K_{IC}}\right)^n \tag{2}$$

where C_{ext} and n are parameters that rock properties and K_{IC} is the rock toughness.

The fracture width is dependent on the net pressureP_{net} , which is the difference between the fracture pressure P_f induced by the injected slurry and the minimum principal stress$\sigma_{\min}$, as

$$P_{net} = P_f - \sigma_{\min} \tag{3}$$

The fracture equation is derived from the integral of the deflection induced by a point-source load over the boundary of a semi-infinite medium [27].

$$w(\vec{r}) = \int_A \frac{(1-\upsilon^2)}{\pi E r} P_{net}\, dA \tag{4}$$

where w is the fracture width, and A is the area the load acts on. $\vec{r}$ denotes the coordinates of the point of interest. The fracture front extends when the stress intensify factor at the front is larger than rock failure toughness. The extension distance along the horizontal direction (x-direction) and the vertical direction (z-direction) is calculated as shown in Equation (5) and Equation (6) respectively.

$$\Delta d_x = v_{front}\Delta t \frac{\frac{K_I}{\sqrt{\Delta h_x}} - K_{IC}}{K_{IC} + \frac{\sigma_{\min} H(x)}{\sqrt{h_z}}}, \ldots\ldots K_I > K_{IC} \tag{5}$$

$$\Delta d_z = v_{front}\Delta t \frac{\frac{K_I}{\sqrt{\Delta h_z}} - K_{IC}}{K_{IC} + \frac{\sigma_{\min} H(x)}{\sqrt{h_z}}}, \ldots\ldots K_I > K_{IC} \tag{6}$$

In the above equation, v_{front} is the maximum velocity at which the fracture front extends. Δt is the time step length. $\Delta h_x$and Δh_z is the dimension of the grid block along x and z-direction respectively, $H(x)$ is the fracture height, varying along the fracture extension direction (x-direction). h_z is the position of the grid block along the vertical direction (z-direction) in the fracture plain.

2.2. Mass/energy transport inside the fracture

The injected slurry is assumed to be a mixture of multiple species, including solid species (proppants) and fluid species (water/gel/additives). The fracture is simulated on a pre-set grid. The dimension along which the fracture extends is set as the x-direction. The fracture grid blocks are allowed to deviate along the direction that is perpendicular to the x-direction. The deviation direction is set as the y-direction. The vertical direction is set as the z-direction.

The general mass balance equation inside the fracture is

$$\frac{\partial \rho}{\partial t} + \nabla\cdot(\rho\vec{v}) + q = 0 \tag{7}$$

where, $\vec{v}$ is velocity, $\rho$is the density and q is the sink/source term.

We consider the fracture to be a thin slit in the Cartesian y-direction and integrate Equation (5) over that width to yield:

$$\frac{\partial}{\partial x}(\rho\vec{v}w) + \frac{\partial}{\partial z}(\rho\vec{v}w) + \frac{\partial(\rho w)}{\partial t} + q = 0 \tag{8}$$

where w is the fracture width.

Slurry fluid and proppant components are conserved. A version of Equation (6) for a fluid component is obtained by defining the fluid mass per unit volume as the product of fluid density and fluid component volume fraction in the overall fluid volume, and defining the fluid velocity as the fluid superficial velocity averaged over the fracture width. The source/sink terms consist of fluid leakoff, the flow of fluid through the porous fracture wall, and flow of fluid between the completed zones along the wellbore (the surroundings) and the fracture. Then:

$$\frac{\partial}{\partial x}\left[\rho_f x_f\left(1-\sum_{i=1}^{N_p} c_p^i\right)\vec{v}_{fl}w\right] + \frac{\partial}{\partial z}\left[\rho_f x_f\left(1-\sum_{i=1}^{N_p} c_p^i\right)\vec{v}_{fl}w\right] + \frac{\partial}{\partial t}\left[\rho_f x_f\left(1-\sum_{i=1}^{N_p} c_p^i\right)w\right] + \rho_f x_f q_{leak} = 0 \tag{9}$$

In the above equation, q_{leak} is the leakoff volume. $N_p$is the number of proppant types. c_p^i is the proppant concentration of the ith type of proppant.

A version of Equation (6) for a proppant component is obtained by defining the proppant mass per unit volume as the product of proppant grain density and proppant volume fraction, and defining the proppant velocity as the proppant superficial velocity averaged over the fracture width. Proppant velocity does vary for each proppant component and does not leak off through the fracture face, so the leakoff term in Equation (7) is absent. Then:

$$\frac{\partial}{\partial x}\left(\rho_p^i c_p^i \vec{v}_p^i w\right) + \frac{\partial}{\partial z}\left(\rho_p^i c_p^i \vec{v}_p^i w\right) + \frac{\partial}{\partial t}\left(\rho_p^i c_p^i w\right) = 0 \tag{10}$$

Proppant is assumed to be incompressible. Because a fracture

occupies a relatively small range of depth, we consider fluid component density in Equation (8) as constant. Then, Equations 7 and 8 become:

$$\frac{\partial}{\partial x}\left[x_f\left(1-\sum_{i=1}^{N_p}c_p^i\right)\vec{v}_{fl}w\right]+\frac{\partial}{\partial z}\left[x_f\left(1-\sum_{i=1}^{N_p}c_{p\_i}\right)\vec{v}_{fl}w\right]+\frac{\partial}{\partial t}\left[x_f\left(1-\sum_{i=1}^{N_p}c_p^i\right)w\right]+x_f q_{leak}=0 \tag{11}$$

And

$$\frac{\partial}{\partial x}(c_p^i\vec{v}_p^i w)+\frac{\partial}{\partial y}(c_p^i\vec{v}_p^i w)+\frac{\partial}{\partial t}(c_p^i w)=0 \tag{12}$$

If we sum Equation (9) over fluid components, Equation (10) over proppant components, and add the results together, we obtain an overall slurry conservation equation:

$$\frac{\partial}{\partial x}\left[\left(1-\sum_{i=1}^{N_p}c_p^i\right)\vec{v}_f+\sum_{i=1}^{N_p}c_p^i\vec{v}_p^i\right]w+\frac{\partial}{\partial z}\left[\left(1-\sum_{i=1}^{N_p}c_p^i\right)\vec{v}_f+\sum_{i=1}^{N_p}c_p^i\vec{v}_p^i\right]w+\frac{\partial w}{\partial t}+q_{leak}=0 \tag{13}$$

We equate the coefficient of w in the length derivatives to the slurry velocity, a weighted sum of fluid and proppant velocities:

$$\vec{v}_{sl}=\left(1-\sum_{i=1}^{N_p}c_p^i\right)\vec{v}_{fl}+\sum_{i=1}^{N_p}c_p^i\vec{v}_p^i \tag{14}$$

Equation (11) then becomes:

$$\frac{\partial}{\partial x}(\vec{v}_{sl}w)+\frac{\partial}{\partial z}(\vec{v}_{sl}w)+\frac{\partial w}{\partial t}+q_{leak}=0 \tag{15}$$

The slurry velocity through the fracture is

$$\vec{v}_{sl}=\frac{w^2}{12\mu_{sl}}\nabla(P_f+\gamma_{sl}z) \tag{16}$$

where γ_{sl} is the gravity term. The approach to calculate the slurry viscosity will be described in the section below. Proppant component and fluid velocities generally differ because proppant is denser than fluid and consists of discrete granules that can interact with each other and with the fracture wall. Therefore, the z-direction velocity of proppant is the sum of the slurry velocity plus a proppant settling velocity that accounts for the difference in fluid and proppant component densities, as

$$v_{p,z}^i=v_{sl}+v_{p,stl}^i \tag{17}$$

where $v_{p,z}^i$ is proppant component velocity and $v_{p,stl}^i$ is proppant component settling velocity. Proppant settling velocity is calculated based on Stoke's law as

$$v_{p,stokes}^i=\frac{\left(\rho_p^i-\rho_{fl}\right)g(d_p^i)^2}{18\mu_{fl}} \tag{18}$$

where $v_{p,stokes}^i$ is the Stoke's velocity and d_p^i is the proppant grain diameter of the ith proppant respectively. Our simulator adopts Friehauf's approach to calculate the settling velocity [28], the proppant settling velocity is the following form:

$$v_{p,stl}^i=v_{p,stokes}^i f(N_{\mathrm{Re}}^i)g_p h(w) \tag{19}$$

where,N_{Re}^i is Reynold's number, $f(N_{\mathrm{Re}}^i)$ captures inertial effects, g_p captures the effect of interfering proppant particles, and $h(w)$ captures the effect of the fracture wall. These expressions, modified for the presence of multiple proppant components, are:

$$f(N_{\mathrm{Re}}^i)=\frac{0.3736\mu_{fl}^{0.57}}{\rho_{fl}^{0.29}\left(\rho_p^i-\rho_{fl}\right)^{0.29}(d_p^i)^{0.86}} \tag{20}$$

$$g_p=-5.9\left(\sum_{i=1}^{N_p}c_p^i\right)^3+8.8\left(\sum_{i=1}^{N_p}c_p^i\right)^2-4.8\sum_{i=1}^{N_p}c_p^i+1 \tag{21}$$

$$h(w)=0.563\left(\frac{d_p^i}{w}\right)^2-1.563\left(\frac{d_p^i}{w}\right)+1 \tag{22}$$

For the direction perpendicular to the gravity vector, the proppant velocity is effected by the fracture wall and other proppant particles. Friehauf modified this velocity by introducing a multiplicative retardation factor for the slurry velocity that accounts for both of these [28]:

$$v_{p,x}^i=C_{ret}(c_p^i,w)v_{sl,x}^i \tag{23}$$

This multiplicative factor is given by:

$$C_{ret}(c_p^i,w)=1+\left(\frac{d_p^i}{w_c}\right)-2.02\left(\frac{d_p^i}{w_c}\right)^2 \tag{24}$$

And

$$\frac{1}{w_c^2}=1.411\left(\frac{1}{(d_p^i)^2}-\frac{1}{w^2}\right)\left(\sum_{i=1}^{N_p}c_p^i\right)^{0.8} \tag{25}$$

Fluid velocity is then obtained from slurry velocity and proppant velocity by rearranging Equation (12):

$$\vec{v}_{fl}=\frac{\vec{v}_{sl}-\sum_{i=1}^{N_p}c_p^i\vec{v}_p^i}{\left(1-\sum_{i=1}^{N_p}c_p^i\right)} \tag{26}$$

The slurry density ρ_{sl} is calculated by weighting the density of the fluid components and the solid components, as

$$\rho_{sl}=\sum_{i=1}^{N_p}c_{pi}\rho_{pi}+\left(1-\sum_{i=1}^{N_p}c_{pi}\rho_{pi}\right)\sum_{i=1}^{N_f}x_{fi}\rho_{fi} \tag{27}$$

In the above equation, $i$refers to the ith component. p and f refers to proppant (solid) and fluid components, respectively. N_p and N_f is the number of proppant species and number of fluid species respectively. c and x is the volume fraction of proppant component and fluid respectively.

3. Integrated finite difference discretization numerical approach

Our simulator is based on uniform grid. The mass/heat transport governing equation is solved in a 2D plane, while the mechanical impact is enforced on the third direction that is normal to the grid plane. Therefore, our simulator conducts 3D simulation of the fracturing process. The grid block (Fig. 1) can be assigned with different properties to account for the heterogeneity of the formation. Our simulator solves the governing equations by integrated finite difference (IFD) method, as proposed by Narasimhan and Witherspoon in 1976 [29].

In this method, the simulation domain is subdivided into sub domains and the governing equations are integrated over a sub domain with flux terms expressed as an integral over the sub domain boundary using the divergence theorem. The definitions of the geometric parameters used in the following derivation of this method. We consider a generalized conservation equation of the form:

$$\frac{\partial M^k}{\partial t}=\nabla\cdot\overline{F}^k+q^k \tag{28}$$

where k refers to conserved quantity, M is quantity per unit volume, F is

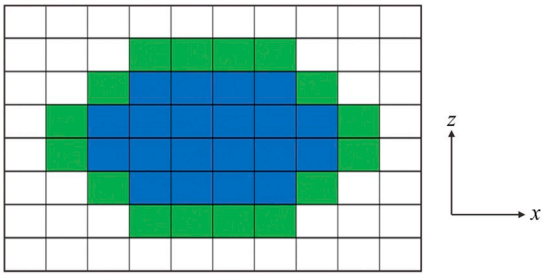

Fig. 1. Concpetual model of fracture on the grid. Green grid blocks refer to newly activated (cracked) grid blocks. Blue grid blocks refer to grid blocks that are cracked in previous time steps.

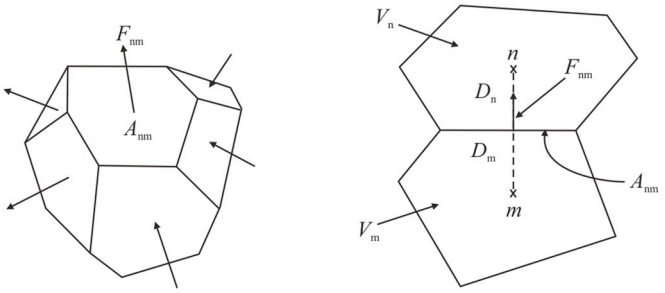

Fig. 2. Conceptual model of integral finite difference method [29,30].

flux, and q is source/sink term. Integrating Equation (28) over a sub domain V_n yields:

$$\frac{\partial}{\partial t}\int_{V_n} M^k dV = \int_{\Gamma_n} \overline{F}^k \cdot \hat{n} d\Gamma + \int_{V_n} q^k dV \tag{29}$$

Integrals over V_n are replaced with averages:

$$\int_{V_n} M^k dV = M_n^k V_n \tag{30}$$

Integrals over the sub domain boundary are replaced with discrete sums over boundary-averaged segments:

$$\int_{\Gamma_n} \overrightarrow{F}^k \cdot \hat{n} d\Gamma = \sum_m A_{nm} \overrightarrow{F}_{nm}^k \tag{31}$$

where subscript n denotes an averaged quantity over V_n, A_{nm} is the boundary segment common to V_n and V_m, double subscript nm denotes an averaged quantity over boundary segment A_{nm}. The time derivative is approximated by the standard first order finite difference approximation. Applying these approximations to Equation (29) yields:

$$[M_n^k]^{l+1} - [M_n^k]^l - \frac{\Delta t}{V_n}\left[\sum_m A_{nm} F_{nm}^k + V_n q_n^k\right] = 0 \tag{32}$$

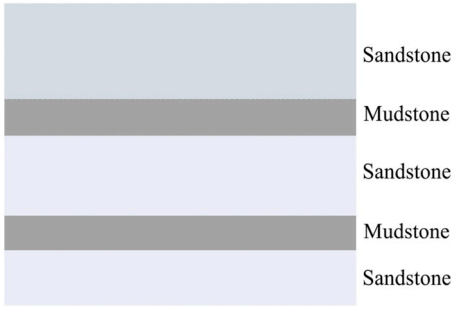

Fig. 4. The profile of the multi-layer formation.

Table 1
Input parameters for the radial fracture case.

Properties	Values	Units
Young's modulus	17.24	GPa
Poisson's ratio	0.25	dimensionless
Biot's coefficient	1.0	dimensionless
Grid block length (x-direction)	10	m
Grid block height (z-direction)	10	m
Injection rate	3.18	m^3/min
Injection time	30	min
Frac fluid viscosity	40	cp

where l is time level.

These governing equations (Equation (32)) expressed in residual vector form are:

$$R(\mathbf{x}^{\mathbf{l+1}}) = 0 \tag{33}$$

where, $\mathbf{x}^{\mathbf{l+1}}$ is the primary variable vector at time level $l+1$.

The time step length $\Delta t$is calculated based on the Courant–Friedrichs–Lewy (CFL) number as

$$C_{FL} = \frac{v_{inj}\Delta t}{\min(\Delta x, \Delta z)} \tag{34}$$

where v_{inj} is the velocity of the fluid in the wellbore, calculated from the wellbore model. Δx and Δz are the grid block length along the x and z direction, respectively. To ensure the convergence, the CFL number should not exceed 1. In this work, it is set to be 0.8 by default.

Fractures extension depend on formation stress field, this stress field will change when a fracture appears by hydraulic fracturing, so the follow-up fractures profile will also change, this phenomena is called stress shadow. We can combine the IDF with Discontinuous Displacement Method (DDM) to describe the stress shadow effect and simulate different stages fractures. DDM is essentially a boundary element type method, it can calculate the induced stress field, this

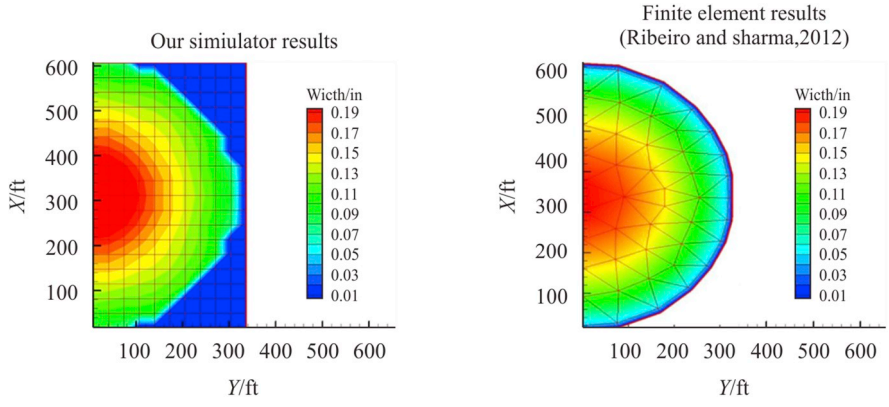

Fig. 3. Simulated fracture width after 30 min injection.

Table 2
Three cases for different mudstone layer thickness.

case	upper mudstone		sandstone		lower mudstone	
	Thickness,m	Stress,MPa	Thickness,m	Stress,MPa	Thickness,m	Stress,MPa
1	15	58	12	52	15	58
2	20	58	12	52	20	58
3	25	58	12	52	25	58

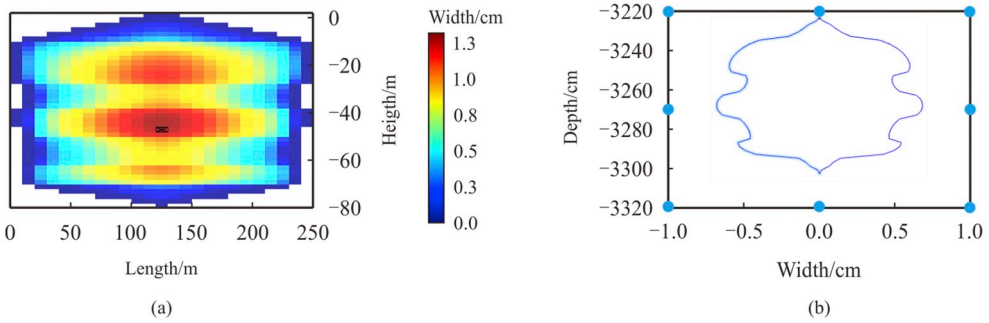

Fig. 5. The fracture profile for case 1 (mudstone thickness is 15 *m*).

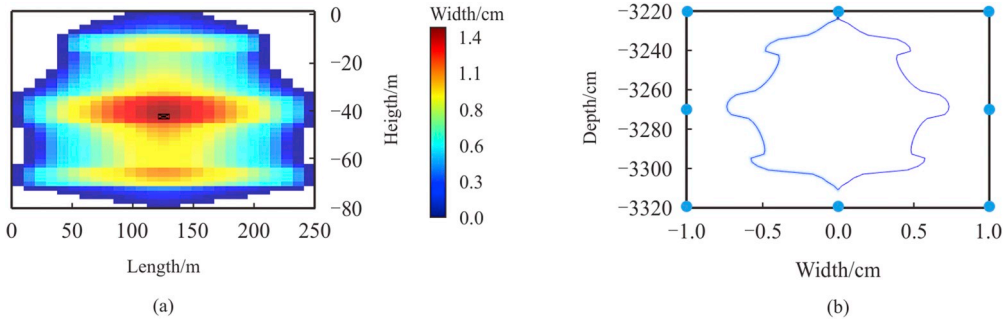

Fig. 6. The fracture profile for case 2 (mudstone thickness is 20 *m*).

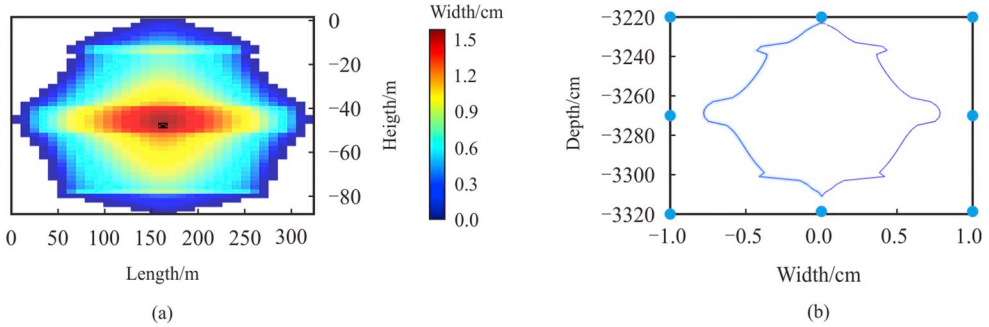

Fig. 7. The fracture profile for case 3 (mudstone thickness is 25 *m*).

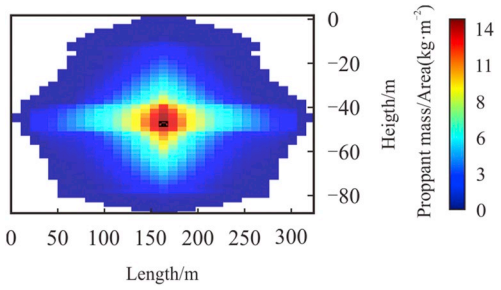

Fig. 8. Proppant distribution strength (proppant mass/area) at near wellbore fracture profile for case 3.

calculated stress field is added to grid blocks in IFD to determine displacement, and the vertical displacement can be defined as fracture width. Tang described the method of how to combine the DDM and another fracture model [20].

4. Validation

We first compare the radial fracture extension problem is a simulation of fracture extension in the horizontal plane with no leakoff, gravity, or temperature effects [31] (see Fig. 2). Fig. 3 shows simulated fracture width after 30 min of injection. The fracture geometry for both models are similar, the fracture width profiles from both simulators are very similar. The fracture half-length from our simulator is about

Table 3
Three cases for different mudstone stress.

case	Upper mudstone		sandstone		Lower mudstone	
	Thickness,m	Stress,MPa	Thickness,m	Stress,MPa	Thickness,m	Stress,MPa
1	15	58	12	52	15	58
2	15	62	12	52	15	62
3	15	72	12	52	15	62

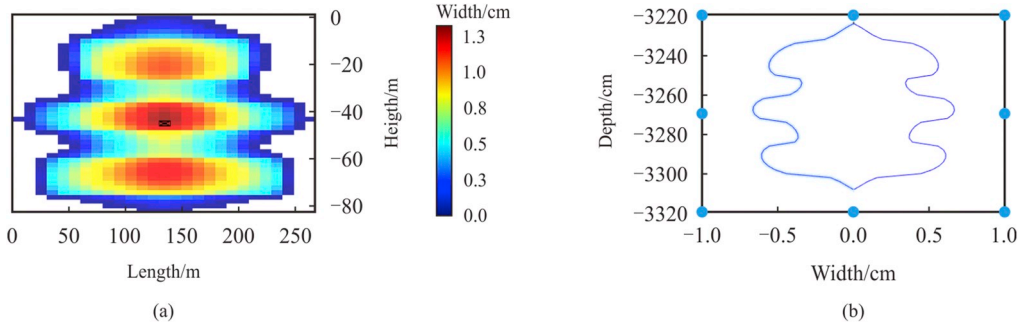

Fig. 9. The fracture profile for case 2 (mudstone stress is 62 MPa).

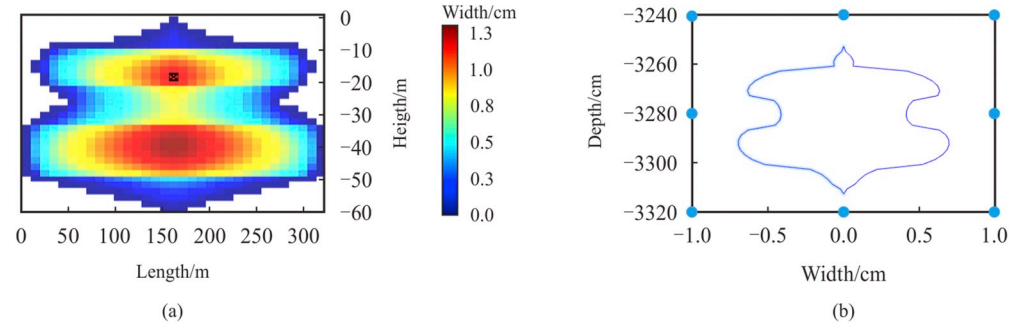

Fig. 10. The fracture profile for case 3 (mudstone stress is 72 MPa).

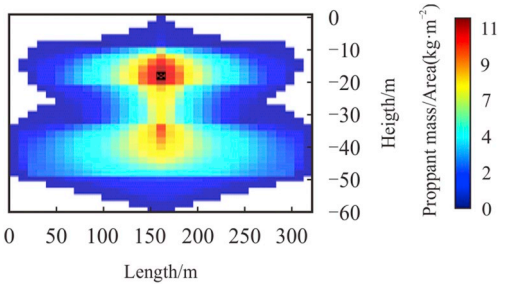

Fig. 11. Proppant distribution strength (proppant mass/area) at near wellbore fracture profile for case 3.

94.5 m (310 ft), the fracture half-length from Ribeiro and Sharma is 100.5 m (330 ft), they are also similar. Ribeiro and Sharma also compared fracture radius versus time to an analytical solution for radial fractures with no leakoff from Geertsma and obtained good agreement [4,31].

5. Field case study

5.1. The mudstone interlayers effect on fractures extension

In this section, we present a series of case study to investigate the impact of thin layers with stress contrast on fracture growth as well as proppant distribution. We run our simulator on a multi-layer reservoir with sandstone layers and mudstone layers appearing in sequence. The mudstone layers play like interlayers in this case study. The perforation (injection point) locates at the sandstone layer in the middle. The conceptual model of the multi-layer formation and the position of perforation is shown in Fig. 4.

Some input parameters as follows, formation pressure is 24 MPa, and formation temperature is 90 °C, perforation layer is between 3269 and 3273 *m*, frac fluid is injected through tubing, tubing ID is 61.98 mm, injection rate is 2.4 m^3/min, total injection volume is 180 m^3, average proppant concentration is 400 kg/m^3, total proppant is 49.2t. The Young's module for sandstone is 41 GPa, the Young's module for mudstone is 48 GPa, and Poisson's ratio for sandstone and mudstone are 0.22 (see Table 1).

5.1.1. Mudstone layer thickness effect for fractures extension

We assume three cases (in Table 2), mudstone thickness is 15 *m*, 20 *m* and 25 *m*. Sandstone stress is 52 MPa, thickness is 12 *m*, and mudstone stress is 58 MPa, so the stress contrast between sandstone and mudstone is 6 MPa. We simulate fractures profile for three cases by our model.

From Figs. 5–7, comparing fracture profiles of three cases, it shows that as the thickness of mudstone layer increase, the resistance of fracture upward extension increase, and it is easier to form a long and wide fracture. fracture length is from 230 *m* to 310 *m*, the maximum fracture width is from 1.3 cm to 1.5 cm, and fracture extension is mainly restricted in sandstone, fracture cannot extend to upper and lower mudstone. Propant transport only in sandstone if fracture cannot

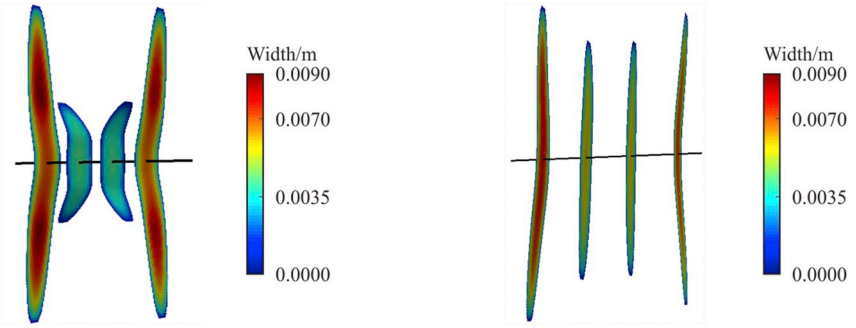

(a) Spacing:20m (b) Spacing:40m

Fig. 12. Three dimension fractures profile at spacing 20 *m* and 40 *m*

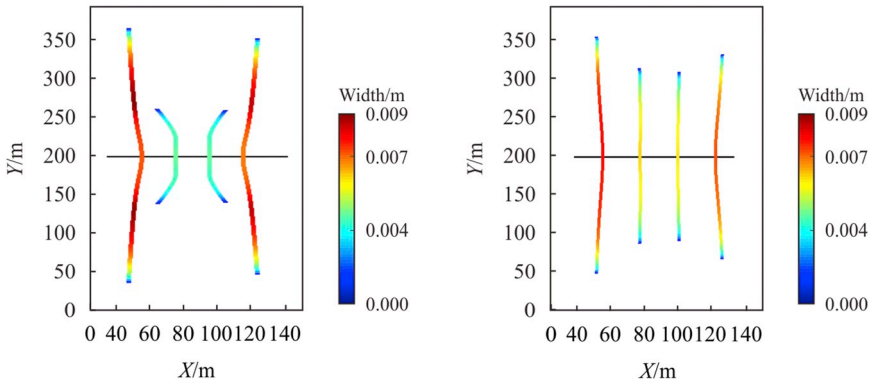

(a) Spacing:20m (b) Spacing:40m

Fig. 13. Map view of fractures profile at spacing 20 *m* and 40 *m*

extend to mudstone, so fractures cannot be the channel between sandstone and upper/lower sandstones. On the other hand, from Fig. 8, although the fracture penetrates the layer above and below, not many proppants enter the sandstone layers above and below. In this sense, when the pumping stops and the fracture close, there will be no effective (propped) fracture in the sandstone layers above and below. This phenomenon is partly because the fracture toughness of mudstone and tight sandstone in this reservoir is close to each other.

5.1.2. Stress contrast between sandstone and mudstone effect for fracture extension

We also assume three cases (in Table 3), mudstone stress is 58 MPa、62 MPa、72 MPa. Sandstone thickness is 12 *m*, mudstone thickness is 15 *m*, sandstone stress is 52 MPa, so the stress contrast between sandstone and mudstone is 6 MPa、10 MPa、20 MPa. We simulate fractures profile for three cases by our model.

The fracture profile for case 1 is Fig. 5. From Figs. 5 and 9 and Fig. 10, we can find that as mudstone stress increase, the resistance for fracture extension increase obviously, and fracture length increase obviously from 230 *m* to 320 *m*. In case 3 where the minimum principal stress of the upper mudstone layer further increases to 72 MPa, the upper layer cannot be penetrated. Due to the increase of the formation stress, the fracture width decreases while the fracture length increases. Meanwhile, a significant amount of proppants settles downward to the lower sandstone layer. In this way, the lower sandstone layer is also propped (see Fig. 11).

5.2. Fractures spacing effect on fractures profile

In this section, we assume four fractures extend simultaneously, formation is homogeneous, rock Young's module is 41 GPa, Poisson ratio is 0.22, injection rate is 3 m^3/min, injection time is 60mins, proppant density is 2650 kg/m^3, frac fluid viscosity is 170cp, frac fluid density is 1100 kg/m^3, and simulate spacing is 10 *m* and 40 *m*. Fig. 12 and Fig. 13 show the 3D fractures profile and map view of fractures profile, the effect of fracture spacing on fracture profile is very obvious, the smaller the fracture spacing, the more obvious the fracture bending, the larger the fracture spacing, the more uniform the fracture extension. The fractures profile is bending when fracture spacing is 20 *m*, and the fractures profile is uniform when fractures spacing increase to 40 *m*.

6. Summary

In this paper, we have developed a practical multi-physical hydraulic fracturing simulator for tight sandstone reservoirs.

(1) The simulator is able to accurately capture the initiation and extension of fractures in complex multi-layer reservoirs. The accuracy of our simulator has been validated by comparing with an analytical solution as well as Ribeiro and Sharma model.
(2) In the reservoir of the Sulige gas field, the minimum principal stress difference between shale and sandstone is 5 ~ 9 MPa. According to our simulation, the fracturing operation will open the shale layer sand and make channels between the upper and the lower sandstone layer. However, proppants cannot always enter the fracked layers. In this way, gel with stronger proppant-carrying capability should be adopted in such formations. On the other hand, wells with fractures that grow into multiple layers may have potential water conning issues, the water from the lower layers may enter the wellbore through the hydraulic fractures at the later stage of production. Regarding this issue, cautions must be taken to frack water-bearing formations, especially when a water-bearing layer is

below the pay zone and the formation stress contrast is not high enough to prevent the penetration of the fracture.

(3) Fracture spacing affect fracture profile obviously, and the smaller the fracture spacing, the more obvious the fracture bending, the larger the fracture spacing, the more uniform the fracture extension.

References

[1] T.K. Perkins, L.R. Kern, Widths of hydraulic fractures, J. Pet. Technol. 13 (1961) 937–949 https://doi.org/10.2118/89-PA.

[2] I.N. Sneddon, The distribution of stress in the neighbourhood of a crack in an elastic solid, Proc. R. Soc. A Math. Phys. Eng. Sci. 187 (1946) 229–260.

[3] R.P. Nordgren, Propagation of a vertical hydraulic fracture, Soc. Petrol. Eng. J. 12 (1972) 306–314 https://doi.org/10.2118/3009-PA.

[4] J. Geertsma, F. De Klerk, A rapid method of predicting width and extent of hydraulically induced fractures, J. Pet. Technol. 21 (1969) 1571–1581 https://doi.org/10.2118/2458-PA.

[5] S.H. Advani, T.S. Lee, J.K. Lee, Three-dimensional modeling of hydraulic fractures in layered media: Part I—finite element formulations, J. Energy Resour. Technol. 112 (1990) 1 https://doi.org/10.1115/1.2905706.

[6] R.G. Baca, R.C. Arnett, D.W. Langford, Modelling fluid flow in fractured-porous rock masses by finite-element techniques, Int. J. Numer. Methods Fluids 4 (1984) 337–348 https://doi.org/10.1002/fld.1650040404.

[7] Z. Chen, Finite element modelling of viscosity-dominated hydraulic fractures, J. Pet. Sci. Eng. 88–89 (2012) 136–144 https://doi.org/10.1016/J.PETROL.2011.12.021.

[8] N. Moes, T. Belytschko, Extended finite element method for cohesive crack growth, Eng. Fract. Mech. 69 (2002) 813–833 https://doi.org/10.1016/S0013-7944(01)00128-X.

[9] N. Moes, J. Dolbow, T. Belytschko, A finite element method for crack growth without remeshing, Int. J. Numer. Methods Eng. 46 (1999) 131–150 https://doi.org/10.1002/(SICI)1097-0207(19990910)46:1<131::AID-NME726>3.0.CO;2-J.

[10] N. Sukumar, N. Moes, B. Moran, T. Belytschko, Extended finite element method for three-dimensional crack modelling, Int. J. Numer. Methods Eng. 48 (2000) 1549–1570 https://doi.org/10.1002/1097-0207(20000820)48:11<1549::AID-NME955>3.0.CO;2-A.

[11] B. Lecampion, An extended finite element method for hydraulic fracture problems, Commun. Numer. Methods Eng. 25 (2009) 121–133 https://doi.org/10.1002/cnm.1111.

[12] T. Mohammadnejad, A.R. Khoei, An extended finite element method for hydraulic fracture propagation in deformable porous media with the cohesive crack model, Finite Elem. Anal. Des. 73 (2013) 77–95 https://doi.org/10.1016/J.FINEL.2013.05.005.

[13] S. Salimzadeh, N. Khalili, A three-phase XFEM model for hydraulic fracturing with cohesive crack propagation, Comput. Geotech. 69 (2015) 82–92 https://doi.org/10.1016/J.COMPGEO.2015.05.001.

[14] K. Wu, J.E. Olson, Simultaneous multifracture treatments: fully coupled fluid flow and fracture mechanics for horizontal wells, SPE J. 20 (2015) 337–346 https://doi.org/10.2118/167626-PA.

[15] K. Wu, J.E. Olson, Mechanics analysis of interaction between hydraulic and natural fractures in shale reservoirs, Unconventional Resources Technology Conference (URTEC). Denver, CO, 2014 https://doi.org/10.15530/URTEC-2014-1922946.

[16] K. Wu, J.E. Olson, Investigation of the impact of fracture spacing and fluid properties for interfering simultaneously or sequentially generated hydraulic fractures, SPE Prod. Oper. 28 (2013) 427–436 https://doi.org/10.2118/163821-PA.

[17] S.L. Crouch, Solution of plane elasticity problems by the displacement discontinuity method. I. Infinite body solution, Int. J. Numer. Methods Eng. 10 (1976) 301–343.

[18] S. Li, X. Li, D. Zhang, A fully coupled thermo-hydro-mechanical, three-dimensional model for hydraulic stimulation treatments, J. Nat. Gas Sci. Eng. 34 (2016) 64–84 https://doi.org/10.1016/J.JNGSE.2016.06.046.

[19] K. Wu, J.E. Olson, M.T. Balhoff, W. Yu, Numerical analysis of promoting more-uniform development of simultaneous multiple fracture propagation in horizontal wells, SPE Prod. Oper. 32 (01) (2017).

[20] H. Tang, P.H. Winterfeld, Y.-S. Wu, Z. Huang, Y. Di, Z. Pan, J. Zhang, Integrated simulation of multi-stage hydraulic fracturing in unconventional reservoirs, J. Nat. Gas Sci. Eng. 36 (2016) 875–892 https://doi.org/10.1016/j.jngse.2016.11.018.

[21] S. Prashanth, K. Wu, K. Joseph, Optimizaiton of simultaneously propagating multiple fractures in hydraulic fracturing to achieve uniform growth using data-based model reduction, Chem. Eng. Res. Des. 136 (2018) 675–686.

[22] X. Guo, K. Wu, C. An, J. Tang, J. Killough, Numerical investigation of effects of subsequent parent well injection on Interwell fracturing interference using reservoir-geomechanics-fracturing modeling, SPE J. (2018) accepted https://doi.org/10.2118/195580-PA.

[23] W. Yu, Y. Xu, R. Weijermars, K. Wu, K. Sepehrnoori, A numerical model for simulating pressure response of well interference and well performance in tight oil reservoirs with complex-fracture geometries using the fast embedded-discrete-fracture-model method, SPE Reservoir Eval. Eng. 21 (02) (2018) 489–502 https://doi.org/10.2118/184825-PA.

[24] W. Yu, Y. Xu, M. Liu, K. Wu, K. Sepehrnoori, Simulation of shale gas transport and production with complex fractures using embedded discrete fracture model, AIChE J. 64 (06) (2018) 2251–2264.

[25] C.H. Yew, X. Weng, Mechanics of Hydraulic Fracturing, second ed., Gulf Professional Publishing, Waltham, MA, 2015.

[26] E.N. Mastrojannis, L.M. Keer, T. Mura, Growth of planar cracks induced by hydraulic fracturing, Int. J. Numer. Methods Eng. 15 (1980) 41–54 https://doi.org/10.1002/nme.1620150105.

[27] A.E.H. Love, E.H. Augustus, A Treatise on the Mathematical Theory of Elasticity, Cambridge University Press, 2013.

[28] K.E. Friehauf, Simulation and Design of Energized Hydraulic Fractures, The University of Texas at Austin, 2009.

[29] T.N. Narasimhan, P.A. Witherspoon, An integrated finite difference method for analyzing fluid flow in porous media, Water Resour. Res. 12 (1976) 57–64 https://doi.org/10.1029/WR012i001p00057.

[30] K. Pruess, A practical method for modeling fluid and heat flow in fractured porous media, Soc. Petrol. Eng. J. 25 (1985) 14–26 https://doi.org/10.2118/10509-PA.

[31] L. Ribeiro, M.M. Sharma, A new three-dimensional, compositional, model for hydraulic fracturing with energized fluids, SPE Annual Technical Conference and Exhibition. Soc. Petrol. Eng, 2012.